Monthly Notices of the ROYAL ASTRONOMICAL SOCIETY

MNRAS **524,** 6004–6014 (2023)
Advance Access publication 2023 July 14

https://doi.org/10.1093/mnras/stad2122

Multiwavelength afterglow emission from bursts associated with magnetar flares and fast radio bursts

Yujia Wei(魏煜佳) [1,2,3★] B. Theodore Zhang(张兵) [4] and Kohta Murase [5,6,7,8,4]

[1] *Key Laboratory of Dark Matter and Space Astronomy, Purple Mountain Observatory, Chinese Academy of Sciences,Nanjing 210023, China*
[2] *School of Astronomy and Space Science, University of Science and Technology of China, Hefei 230026, China*
[3] *School of Astronomy & Space Science, Nanjing University, Nanjing 210023, China*
[4] *Center for Gravitational Physics and Quantum Information, Yukawa Institute for Theoretical Physics, Kyoto University, Kyoto 606-8502, Japan*
[5] *Department of Physics, The Pennsylvania State University, University Park, PA 16802, USA*
[6] *Department of Astronomy & Astrophysics, The Pennsylvania State University, University Park, PA 16802, USA*
[7] *Center for Multimessenger Astrophysics, Institute for Gravitation and the Cosmos, The Pennsylvania State University, University Park, PA 16802, USA*
[8] *School of Natural Sciences, Institute for Advanced Study, Princeton, NJ 08540, USA*

Accepted 2023 July 7. Received 2023 June 10; in original form 2023 January 26

ABSTRACT

Magnetars have been considered as progenitors of magnetar giant flares (MGFs) and fast radio bursts (FRBs). We present detailed studies on afterglow emissions caused by bursts that occur in their wind nebulae and surrounding baryonic ejecta. In particular, following the bursts-in-bubble model, we analytically and numerically calculate spectra and light curves of such afterglow emission. We scan parameter space for the detectability of radio signals, and find that a burst with $\sim 10^{45}$ erg is detectable with the Very Large Array or other next-generation radio facilities. The detection of multiwavelength afterglow emission from MGFs and/or FRBs is of great significance for their localization and revealing their progenitors, and we estimate the number of detectable afterglow events.

Key words: stars: neutron – fast radio bursts.

1 INTRODUCTION

Magnetars are young highly magnetized neutron stars (e.g. Kaspi & Beloborodov 2017, for a review). Their emission is typically observed at X-ray and soft gamma-ray bands, which are powered by the decay of magnetic fields. The magnetars can be phenomenologically divided into two classes, which are anomalous X-ray pulsars and soft gamma repeaters (SGRs), and SGRs are characterized by weak and recurring short bursts. They are known to produce giant flares in the gamma-ray band, which we call magnetar giant flares (MGFs). A small fraction of gamma-ray bursts (GRBs) originate from MGFs, and examples include GRB 790305B (e.g. Mazets et al. 1979), GRB 980 827 (e.g. Hurley et al. 1999; Mazets et al. 1999), and GRB 041 227 (e.g. Palmer et al. 2005; Frederiks et al. 2007) for Galactic events, and GRB 200415A has been thought to be a most likely extragalactic MGF (e.g. Minaev & Pozanenko 2020; Yang et al. 2020; Roberts et al. 2021; Svinkin et al. 2021; Zhang et al. 2022).

Magnetars have been thought to be the most promising progenitors of fast radio bursts (FRBs; e.g. Petroff, Hessels & Lorimer 2019; Zhang 2022, for reviews). In 2020, FRB 200 428 detected by CHIME (CHIME/FRB Collaboration 2020) and STARE2 (Bochenek et al. 2020) was confirmed to be associated with a Galactic magnetar SGR 1935+2154. This evidence indicates that magnetars are at least one of the origins of FRBs.

Detecting multiwavelength counterparts of FRBs is crucial for better understanding the progenitors and mechanisms, and more dedicated multiwavelength search campaigns are necessary (Nicastro et al. 2021). However, theoretical predictions are highly model dependent. Among various possibilities, possible connections between FRBs and gamma-ray transients have often been discussed (e.g. Popov & Postnov 2010; Zhang 2016; Murase, Mészáros & Fox 2017), but clear associations have not been established so far (e.g. DeLaunay et al. 2016; Acciari et al. 2018; Martone et al. 2019; Venere et al. 2021). Detecting longer-lasting afterglow emission from outflows launched with transient activities is also helpful for identifying the FRB counterparts. Some studies have been proposed to predict the detectability of afterglow emission based on GRB-like models. For example, Yi, Gao & Zhang (2014) studied multiwavelength afterglows from GRB-like outflows, and Lin & Totani (2020) studied the detectability of afterglows in light of the binary neutron star merger model for FRBs. Li et al. (2022) discussed a possible connection between FRB 180916B and a possible optical counterpart AT2020hur of FRB assuming a collimated outflow.

In this work, following the bursts-in-bubble model proposed by Murase, Kashiyama & Mészáros (2016), we study week-to-month scale afterglow emission caused by outflows that may be associated with MGFs and/or FRBs. Magnetars may inject rotation and/or magnetic energy into their nebulae. If there is a burst (e.g. FRB and/or MGF) inside such a nebula, an associated outflow will sweep the nebula with a mass of $\sim 10^{-9}$–$10^{-5}\,M_\odot$ (Murase et al. 2016), forming trans-relativistic ejecta. This may be consistent with radio afterglow emission observed from SGR 1806−20, for which a fading

★ E-mail: yjwei@pmo.ac.cn

© 2023 The Author(s)
Published by Oxford University Press on behalf of Royal Astronomical Society

Downloaded from https://academic.oup.com/mnras/article/524/4/6004/7224608 by guest on 09 August 2023

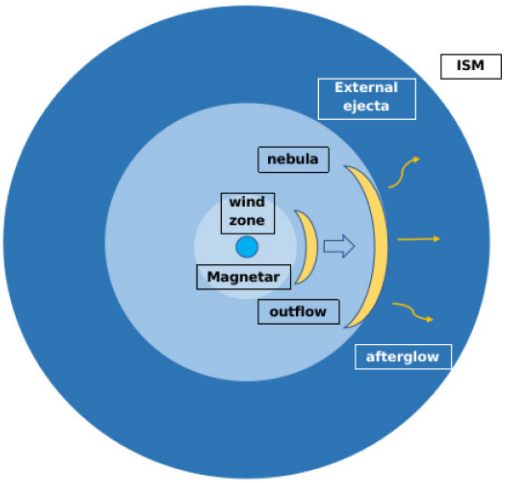

(a)

Figure 1. A schematic picture of afterglow emission following a burst, which may be associated with an MGF and/or FRB. A magnetar is surrounded by its wind nebula and baryonic SN/merger ejecta (external baryonic ejecta). A burst-driven outflow sweeps the nebula and forms a trans-relativistic shell, which is quickly decelerated by the dense baryonic ejecta, and afterglow emission is generated by the refreshed forward shock.

radio source VLA J180839-202439 was identified (Gaensler & Slane 2006). According to Kaspi & Beloborodov (2017), of the 23 magnetars identified, eight are reliably related to supernova (SN) remnants. If magnetars are as young as ∼10–100 yr, it is rather natural to expect that the outflow interacts with dense baryonic SN ejecta.

We use both analytical and numerical methods to calculate the dynamic evolution of the refreshed forward shock and the corresponding afterglow emission. We also study whether such afterglow emission from a nearby galaxy like M 81 can be detected in the radio, optical, and X-ray bands. We then scan the parameter space to find the detection horizon for current and next-generation radio telescopes, which include the Atacama Large Millimeter/sub-millimeter Array (ALMA), the Very Large Array (VLA), the Square Kilometer Array (SKA), and the Next Generation Very Large Array (ngVLA). Finally, we calculate the expected number of afterglow events detected with these radio telescopes.

We use notations as $Q_x = Q/10^x$ in the CGS unit except $t_{\rm yr} \equiv (t/1\,{\rm yr})$ and $M_{\rm ej,1M_\odot} = M_{\rm ej}/1{\rm M}_\odot$.

2 MODEL

In this section, we describe the details of the model and methods that are used to calculate multiwavelength afterglow emission.

In Fig. 1, we show the schematic picture of the bursts-in-bubble model (Murase et al. 2016). The magnetic and/or spin-down activity of magnetars powers relativistic winds that are accelerated mainly in the wind zone between the light cylinder and the nebula, leading to the formation of a wind bubble embedded in the SN or merger ejecta. Then an impulsive burst that may be associated with an MGF and/or FRB may be accompanied by an outflow that will sweep up the nebula. The pre-existing non-thermal particles in the nebula may be boosted by the outflow, which may lead to the gamma-ray emission (e.g. Lyubarsky 2014; Murase et al. 2016). The swept-up nebula can still be trans-relativistic, which may eventually interact with the baryonic SN/merger ejecta, by which afterglow emission is expected, as shown in Fig. 1.

2.1 Dynamics

At early times, the merged shell is in the free-expansion phase where the velocity $v_{\rm s}$ of the forward shock keeps constant and its value is equal to the initial velocity of the merged shell. During this free-expansion phase, the radius of the shock is

$$r_{\rm s} \approx v_0 t \simeq 2.6\times10^{15}\,{\rm cm}\,t_5, \quad (t \le t_{\rm dec}), \tag{1}$$

where t is the observation time after the burst and $v_0 \simeq 2.6\times10^{10}$ cm s^{-1} is the initial velocity of the shock corresponding to the initial Lorentz factor $\Gamma_0 = 2$. When the accumulated mass is equal to the initial mass of the merged shell, the merged shell begins to decelerate. This deceleration time $t_{\rm dec}$ and the corresponding deceleration radius $r_{\rm dec}$ are (e.g. Nakar & Piran 2011),

$$\begin{aligned} r_{\rm dec} &= \left(\frac{3\mathcal{E}_k}{4\pi n_{\rm ext} m_p c^2 \Gamma_0^2}\right)^{1/3} \simeq 1.6\times10^{15}\,{\rm cm}\,\mathcal{E}_{k,47}^{1/3} n_{\rm ext,3}^{-1/3}, \\ t_{\rm dec} &= \frac{r_{\rm dec}}{v_0} \simeq 6.1\times10^4\,{\rm s}\,\mathcal{E}_{k,47}^{1/3} n_{\rm ext,3}^{-1/3}, \end{aligned} \tag{2}$$

where $\mathcal{E}_k$ is the kinetic energy of the merged shell, $n_{\rm ext}$ is the number density of the external baryonic ejecta. This number density can be estimated through the following formula

$$\begin{aligned} n_{\rm ext} &= \frac{3M_{\rm ext}}{4\pi R_{\rm ext}^3 m_p} \\ &\simeq 2.9\times10^5\,{\rm cm}^{-3}\,M_{\rm ext,1M_\odot} V_{\rm ext,8.5}^{-3} T_{\rm age,10\,yr}^{-3}, \end{aligned} \tag{3}$$

where $R_{\rm ext} = V_{\rm ext} T_{\rm age} \simeq 1.0\times10^{17}$ cm $V_{\rm ext,8.5} T_{\rm age,10\,yr}$ is the radius of SN ejecta, $V_{\rm ext}$ is the velocity of SN ejecta, $M_{\rm ext}$ is the mass of SN ejecta, and $T_{\rm age}$ is the age of the magnetar at the time of a burst.

During the deceleration phase, the evolution of the forward shock following the Sedov–Taylor solution, where the shock velocity is

$$v_{\rm s} \simeq 3.7\times10^9{\rm cm\,s^{-1}}\,\mathcal{E}_{k,47}^{1/5} n_{\rm ext,3}^{-1/5} t_6^{-3/5}, \quad (t > t_{\rm dec}), \tag{4}$$

and the shock radius $r_{\rm s}$ is

$$r_{\rm s} \simeq 1.0\times10^{16}\,{\rm cm}\,\mathcal{E}_{k,47}^{1/5} n_{\rm ext,3}^{-1/5} t_6^{2/5}, \quad (t > t_{\rm dec}). \tag{5}$$

Note the above Sedov–Taylor solution will not be valid when the radius of the forward shock is larger than the extension of the external baryonic ejecta, which means $r_{\rm s}$ should be smaller than $R_{\rm ext}$.

The above estimates are not accurate in the trans-relativistic case and become invalid in the relativistic case, where the shock propagates a distance of ${\rm d}r = \beta c/(1-\beta){\rm d}t$ during the time interval ${\rm d}t$ when measured in the observer frame. In order to have better modelling of the transition from the free-expansion phase to the deceleration phase, we numerically solve the dynamical evolution of the interacting shell (e.g. Nava et al. 2013). The total energy of the interacting shell is

$$\mathcal{E}_{\rm tot} = \Gamma M_{\rm ej} c^2 + \Gamma m_{\rm ext} c^2 + \frac{\hat{\gamma}\Gamma^2 - \hat{\gamma} + 1}{\Gamma}\mathcal{E}'_{\rm int}, \tag{6}$$

where $\mathcal{E}_{\rm tot}$ is the total energy, Γ is the Lorentz factor of the merged shell, $M_{\rm ej}$ is the mass of the merged shell, $m_{\rm ext}$ is the mass of accumulated external baryonic ejecta, $\hat{\gamma} = (4+\Gamma^{-1})/3$ is the adiabatic index, and $\mathcal{E}'_{\rm int}$ is the internal energy. Considering energy conservation, i.e. ${\rm d}\mathcal{E}_{\rm tot} = {\rm d}m_{\rm ext}c^2$ where the change of $\mathcal{E}_{\rm tot}$ is due to the accumulation of the external baryonic ejecta, we can establish the differential equation to describe the evolution of Γ. See the details in Zhang et al. (2021).

Throughout the work we assume $\Gamma_0 = 2$, corresponding to $v_0 \simeq 0.87c$. We compare the analytical (green lines) and numerical (yellow lines) dynamic evolution for $\mathcal{E}_k = 10^{47.5}$ erg and $T_{\rm age} = 100$ yr in Fig. 2. For analytical curves, we do not show the result in the

Downloaded from https://academic.oup.com/mnras/article/524/4/6004/7224608 by guest on 09 August 2023

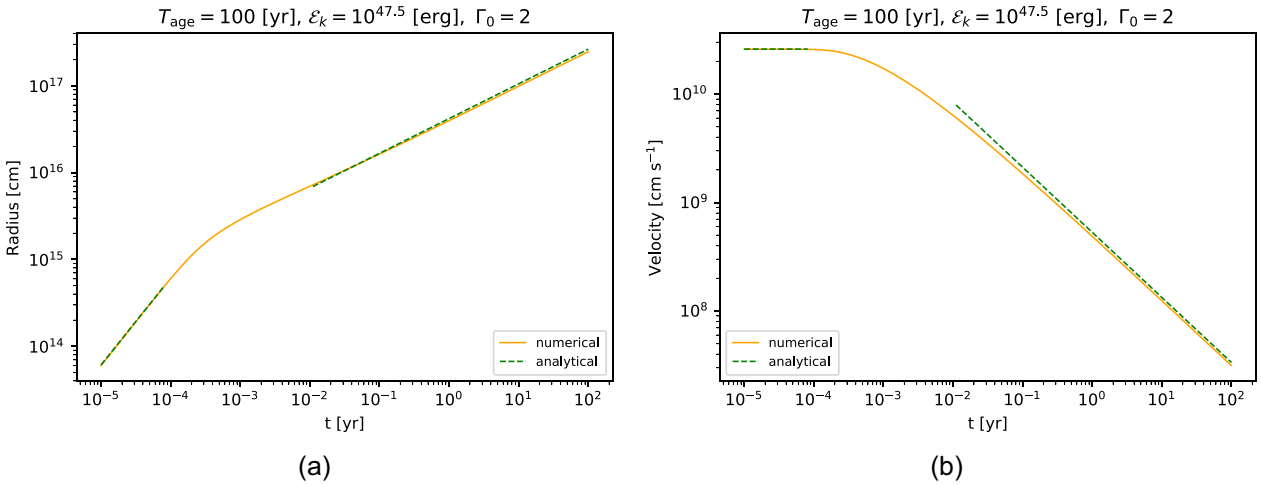

Figure 2. Analytical and numerical results for the thin-shell approximation on the dynamic evolution of the forward shock caused by interaction with the external baryonic ejecta. The yellow line represents the numerical result, while the green line indicates the analytical result.

transition phase since it is not accurate. However, the free expansion phase and the deceleration phase could be smoothly connected via solving the dynamical evolution of the interacting shell numerically.

In above case, we adopt the thin-shell approximation of the inner ejecta, which are formed when energetic relativistic outflow merged into the nebula. According to the burst-in-bubble model (Murase et al. 2016), after the burst, the shocked nebula is highly compressed and confined into a thin layer with a width depending on the ratio of the pressure between the energetic relativistic outflow and the nebula. To take into account the thick shell evolution, we modify the differential equation on the evolution of the Lorentz factor equation A2 used in Zhang et al. (2021). In particular, we use the method proposed in Nava et al. (2013), and assume that the ejecta have a width of $\Delta R_{\rm ej} = R_{\rm nb}/12\Gamma_0^2$ measured in the engine frame and $t_{\rm cross} = \Delta R_{\rm ej}/v_0$ is the crossing time of the reverse shock without spreading. The emission will peak at $t_\times = \max[t_{\rm cross}, t_{\rm dec}]$.

2.2 Synchrotron emission

Magnetic fields may be amplified via the shock, as indicated in GRBs (e.g. Mizuno et al. 2014; Santana, Barniol Duran & Kumar 2014). The downstream magnetic field is estimated to be

$$B_{\rm fs} \approx (9\pi\epsilon_B n_{\rm ext} m_p {v_s}^2)^{1/2} \simeq 0.026\ {\rm G}\ \mathcal{E}_{k,47}^{1/5} n_{\rm ext,3}^{3/10} t_6^{-3/5} \epsilon_{B,-3}^{1/2}, \quad (7)$$

where ϵ_B is the magnetic energy fraction transferred from post-shock thermal energy. The minimum Lorentz factor of the accelerated electron is

$$\gamma_{\rm m} - 1 \approx \max\left[1, \frac{m_p\epsilon_{\rm e}(s-2)}{2m_e f_e(s-1)}\left(\frac{v_s}{c}\right)^2\right] \simeq \max\left[1, 0.24\ \mathcal{E}_{k,47}^{2/5} n_{\rm ext,3}^{-2/5} t_6^{-6/5} \epsilon_{e,-1} f_{e,0}^{-1}\right], \quad (8)$$

where $s = 2.2$ is the spectral index, $\epsilon_{\rm e}$ is the fraction of post-shock thermal energy transferred to electron energy, and $f_{\rm e}$ is the fraction of thermal electrons accelerated to the non-thermal distribution. Note that the minimum Lorentz factor is fixed to $\gamma_{m,\rm min} = 2$ in the deep-Newtonian phase (e.g. Huang & Cheng 2003; Granot et al. 2006; Sironi & Giannios 2013). The corresponding minimum synchrotron frequency is

$$\nu_{\rm m} = \frac{3}{4\pi}\gamma_m^2\frac{eB_{\rm fs}}{m_e c} \simeq 1.6\times10^5\ {\rm Hz}\ \mathcal{E}_{k,47} n_{\rm ext,3}^{-1/2} t_6^{-3} \epsilon_{B,-3}^{1/2} \epsilon_{e,-1}^2 f_{\rm e,0}^{-2}, \quad (9)$$

where e is the electron charge. Note, we use $\gamma_{\rm m} = 1 + \frac{m_p\epsilon_e(s-2)}{2m_e f_e(s-1)}\left(\frac{v_s}{c}\right)^2$ to derive the second line of above equation but here $\gamma_{\rm m}$ should be 2. The synchrotron cooling frequency is

$$\nu_c = \frac{3}{4\pi}\gamma_c^2\frac{eB_{\rm fs}}{m_e c} \simeq 1.5\times10^{17}\ {\rm Hz}\ \mathcal{E}_{k,47}^{-3/5} n_{\rm ext,3}^{-9/10} t_6^{-1/5} \epsilon_{B,-3}^{-3/2}, \quad (10)$$

where $\gamma_c = 6\pi m_e c/(\sigma_T B_{\rm fs}^2 t)$ is the synchrotron cooling Lorentz factor. The maximum synchrotron frequency is

$$\nu_{\rm max} = \frac{3}{4\pi}\gamma_{\rm max}^2\frac{eB_{\rm fs}}{m_e c} \simeq 1.3\times10^{20}\ {\rm Hz}\ \mathcal{E}_{k,47}^{2/5} n_{\rm ext,3}^{-2/5} t_6^{-6/5}, \quad (11)$$

where $\gamma_{\rm max} = \sqrt{9\pi v_s^2 e/(10\sigma_T B_{\rm fs} c^2)}$ is the maximum Lorentz factor.

The synchrotron peak flux $F_\nu^{\rm max}$ is

$$F_\nu^{\rm max} \simeq 0.6\frac{\sqrt{3}e^3 B_{\rm fs}}{m_e c^2}\frac{4\pi r_s^3 f_e n_{\rm ext}}{3\times4\pi d_{\rm L}^2}\begin{cases}1 & \beta \gg \beta_{\rm DN}\\ \left(\frac{\beta^2}{\beta_{\rm DN}^2}\right)^{\frac{s-1}{2}} & \beta \ll \beta_{\rm DN}\end{cases} \quad (12)$$

where $d_{\rm L}$ is the luminosity distance from the observer to the source and $\beta_{\rm DN} = \sqrt{(2m_e f_e(s-1))/(m_p\epsilon_e(s-2))} \simeq 0.26 f_{e,0}^{1/2}\epsilon_{e,-1}^{-1/2}$ is the critical velocity below which the interacting shell is in the deep-Newtonian phase (e.g. Sironi & Giannios 2013; Matsumoto & Piran 2021). Note that when $t = t_{\rm DN} \simeq 3.0\times10^5$ s $\mathcal{E}_{k,47}^{1/3} n_{\rm ext,3}^{-1/3} f_{e,0}^{-5/6} \epsilon_{e,-1}^{5/6}$, the interacting shell will enter into the deep-Newtonian regime.

Besides, synchrotron self-absorption (SSA) is important for the attenuation of low-frequency synchrotron emission. The SSA optical depth can be estimated by $\tau_{\rm ssa}(\nu) = \int\alpha_\nu {\rm d}s$, where α_ν is the SSA coefficient and the integral is along the width of the shocked region. We can then get the SSA frequency ν_a by using $\tau_{\rm ssa}(\nu_a) = 1$, and we have

$$\nu_a \simeq 7.3\times10^8\ {\rm Hz}\ \mathcal{E}_{k,47}^{1/5} n_{\rm ext,3}^{(3s+22)/[10(s+4)]} t_6^{(-3s-2)/[5(s+4)]} \times\epsilon_{B,-3}^{(s+2)/[2(s+4)]} f_{e,0}^{2/(s+4)}, \quad (13)$$

Downloaded from https://academic.oup.com/mnras/article/524/4/6004/7224608 by guest on 09 August 2023

for $s = 2.2$ and $\gamma_{\rm m} = 2$ in the deep-Newtonian phase. Note that the number of electrons contributing to the SSA process in the deep-Newtonian phase should be corrected accordingly similar to equation (12). The synchrotron emission spectrum can be analytically calculated as

$$F_\nu = F_\nu^{\rm max} \begin{cases} \left(\frac{\nu}{\nu_m}\right)^2 \left(\frac{\nu_a}{\nu_m}\right)^{-s/2-2} & \nu \le \nu_m \\ \left(\frac{\nu}{\nu_a}\right)^{5/2} \left(\frac{\nu_a}{\nu_m}\right)^{-(s-1)/2} & \nu_m < \nu \le \nu_a \\ \left(\frac{\nu}{\nu_m}\right)^{-(s-1)/2} & \nu_a < \nu \le \nu_c \\ \left(\frac{\nu}{\nu_c}\right)^{-s/2} \left(\frac{\nu_c}{\nu_m}\right)^{-(s-1)/2} & \nu_c < \nu < \nu_{\rm max} \end{cases}, \quad (14)$$

in the slow cooling case.

The free–free (FF) absorption is also important when the density of the external baryonic ejecta are so high that free electrons jump to higher-energy states via absorbing low-energy photons. The corresponding optical depth is (e.g. Lang 1999; Murase et al. 2017)

$$\tau_{\rm ff}(\nu) \simeq 8.5 \times 10^{-28}\, \bar{Z}^2 (R_{\rm ext} - r_s) \left(\frac{\nu}{10^{10}\,{\rm Hz}}\right)^{-2.1} n_e n_i \times \left(\frac{T_{\rm ext}}{10^4\,{\rm K}}\right)^{-1.35} \left(\frac{1 - e^{-h\nu/kT_{\rm ext}}}{h\nu/kT_{\rm ext}}\right), \quad (15)$$

where $\bar{Z} = 1$ is the average charge number, $T_{\rm ext}$ is the temperature of the external baryonic ejecta, $R_{\rm ext}$ is the size of the external baryonic ejecta, $n_{\rm e}$ is the free electron number density, and $n_{\rm i}$ is the ion number density. In the singly ionized state, we have $n_{\rm e} = n_{\rm ext}/\mu_{\rm e}$, and we assume $\mu_{\rm e} = 1$ for simplicity. Then we take into account the FF absorption by multiplying $\exp(-\tau_{\rm ff})$.

2.3 Numerical calculations

In the following, we describe the details of our numerical calculations. We employ the numerical code developed initially for GRB afterglows (Murase et al. 2011; Asano, Murase & Toma 2020; Zhang et al. 2021), but modified it to treat the non-relativistic regime self-consistently.[1] We obtain the steady-state electron distribution by solving the kinetic equation in the momentum space

$$\frac{\partial}{\partial p_{\rm e}} \left(n_{p_e}(t) \frac{{\rm d}p_{\rm e}}{{\rm d}t} \right) + \frac{n_{p_e}(t)}{t_{\rm esc}} = \dot{n}^{\rm inj}_{p_e}(t), \quad (16)$$

where $n_{p_e}(t) = 4\pi p_e^2 f_{p_e}(t)$ is the number density of electrons per momentum bin, ${\rm d}p_e/{\rm d}t = p_e t_{\rm cool}^{-1}$ is the electron cooling rate and $\dot{n}^{\rm inj}_{p_e}(t) \propto p_e^{-s} \exp\left(-p_e/p_{e,\rm max}\right)$ for $p_{\rm e} > p_{\rm e,min}$ is the electron injection rate which follows a power-law distribution with exponential cutoff at the maximum momentum $p_{\rm e,max}$. The value of the minimum momentum $p_{\rm e,\,min}$ is determined with equation (8) and the value of $p_{\rm e,max}$ could be determined by $\gamma_{\rm max}$ as mentioned in equation (11). The total number of electrons is normalized by matter conservation $N_{\rm e} = (4\pi/3) r_{\rm s}^3 n_{\rm ext} f_{\rm e}$, where $n_{\rm e} \approx N_{\rm e}/(4\pi r_{\rm s}^2 t_{\rm dyn} \beta_{\rm s} c)$ is the comoving frame electron number density in the shocked region and $t_{\rm dyn} \approx \Gamma_{\rm s} t$ is the comoving frame dynamical time-scale. The advantage of using equation (16) is that the number of electrons still follows power-law distribution even in the deep-Newtonian phase when $\gamma_{\rm m} < 2$. In the deep-Newtonian phase, the minimum electron momentum $p_{\rm e,min}$ dominates the total number of electrons, while only electrons with Lorentz factor $\gamma_{\rm e} \gtrsim 2$ contribute to the synchrotron emission. In the no escape limit where $t_{\rm esc} = \infty$, the electron distribution can be determined from the following function (e.g. Dermer & Menon 2009; Murase et al. 2011; Zhang et al. 2021),

$$n_{p_e}(t) = \frac{1}{p_e t_{\rm cool}^{-1}} \int_{p_e}^{\infty} dp'_e \dot{n}^{\rm inj}_{p'_e}(t), \quad (17)$$

where $t_{\rm cool}^{-1} = t_{\rm syn}^{-1} + t_{\rm IC}^{-1} + t_{\rm ad}^{-1}$ including synchrotron cooling, inverse-Compton cooling and adiabatic cooling, respectively. Once we get the non-thermal electron distribution, we can calculate the synchrotron emission. The effect of SSA and FF is self-consistently considered in the numerical calculations.

[1]The code will be made public as a part of the GRB code used in Asano et al. (2020) and Zhang et al. (2021).

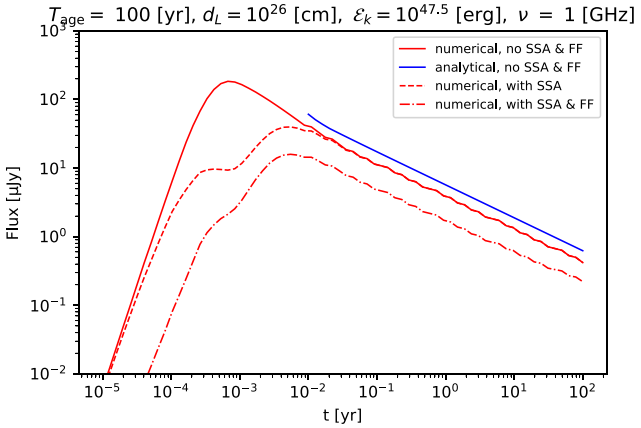

(a)

Figure 3. Light curves at $\nu = 1$ GHz calculated with both analytical (blue lines) and numerical (red lines) methods for an external baryonic density of $n_{\rm ext} \simeq 2900\ {\rm cm}^{-3}$. The solid lines represent the results without considering SSA and FF absorption. The dashed line considers the effect of SSA absorption only. In the dash–dotted line, both SSA and FF absorption are taken into account. The microphysical parameters used here are $s = 2.2, f_{\rm e} = 0.05, \epsilon_{\rm e} = 0.01$, and $\epsilon_B = 0.001$.

2.4 Comparison between the analytical and numerical method

We compare the resulting synchrotron light curves at $\nu = 1$ GHz calculated with both analytical and numerical methods for the thin-shell approximation in Fig. 3. For demonstrative purposes, we assume the kinetic energy is $\mathcal{E}_k = 10^{47.5}$ erg with a luminosity distance of $d_{\rm L} = 10^{26}$ cm and an initial Lorentz factor of $\Gamma_0 = 2$.

In Fig. 3, the light curves are calculated with $T_{\rm age} = 100$ yr where the corresponding external baryonic number density is $n_{\rm ext} \simeq 2900\,{\rm cm}^{-3}$. We can see the consistency of the flux at deceleration phase between numerical (red-solid line) and analytical (blue-solid line) light curves without absorption. We do not show the analytical light curves at the early times since the calculation of analytical method in early time is not accurate. Note that when $t \approx 1.7 \times 10^{-2}$ yr, the shock velocity $\beta_{\rm s}$ becomes smaller than $\beta_{\rm DN} \approx 0.18$. We show the effect of both FF absorption and SSA for the numerical light curve (red dash–dotted line), which is important at the early times. When the density of the external baryonic matter becomes larger, which usually occurred at smaller $T_{\rm age}$, the FF absorption would be more significant.

Downloaded from https://academic.oup.com/mnras/article/524/4/6004/7224608 by guest on 09 August 2023

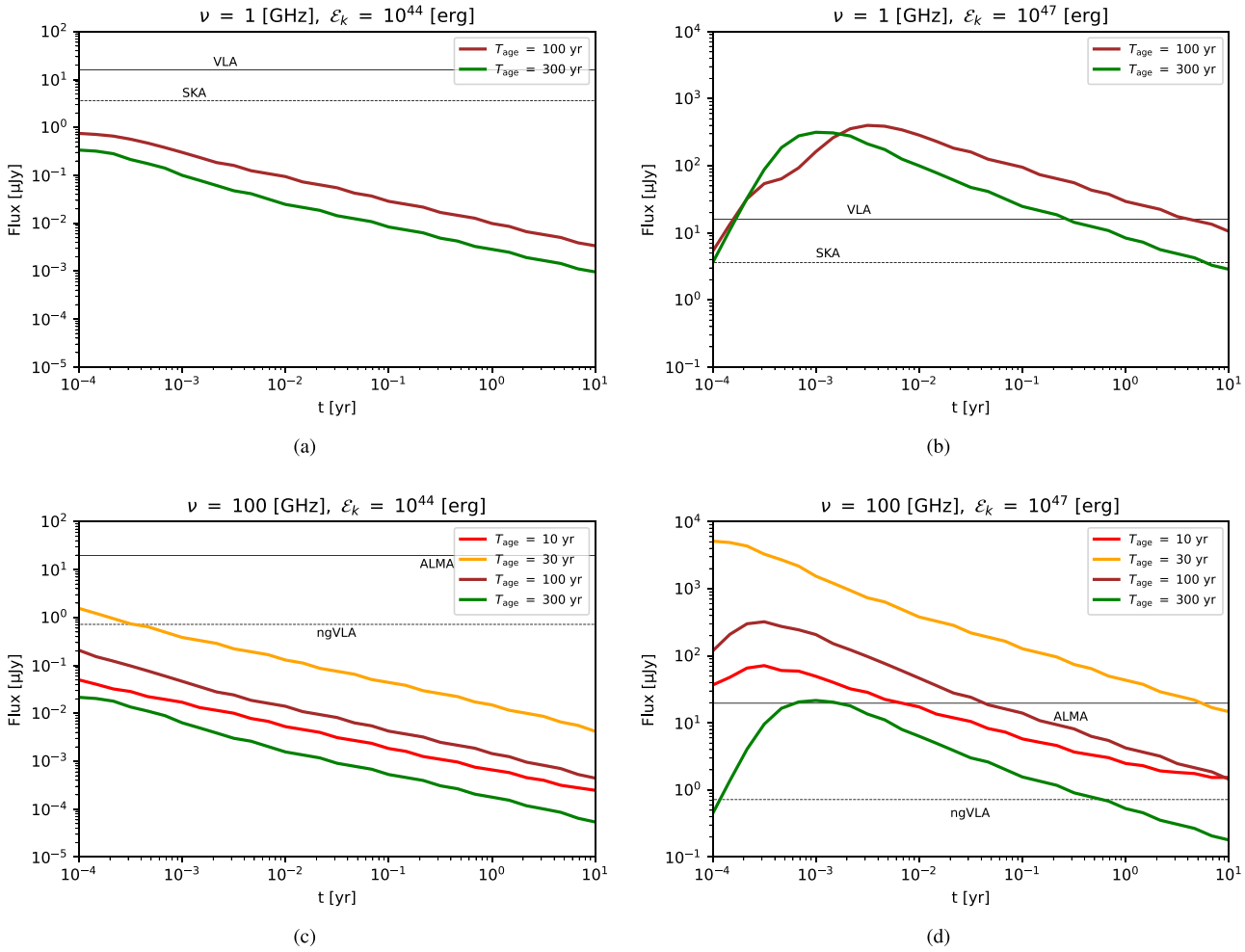

Figure 4. Light curves of afterglow emission at 1 (upper panels) and 100 GHz (lower panels), respectively. The light curves are calculated for different values of $T_{\rm age}$, as indicated in the caption. We show the sensitivity curves of VLA (solid line) and SKA (dashed line) at 1 GHz in the upper panels and those of ALMA (solid line) and ngVLA (dashed line) at 100 GHz in the lower panels. We show the light curves with $\mathcal{E}_k = 10^{44}$ erg (left-hand panels) and $\mathcal{E}_k = 10^{47}$ erg (right-hand panels), respectively. Note that the light curves at the 1 GHz band are significantly reduced when $T_{\rm age} \lesssim 30$ yr due to strong FF absorption, which are not shown in the upper panels. The corresponding physical parameters are $\Gamma_0 = 2$, $d_{\rm L} = 4$ Mpc, $s = 2.2$, $f_{\rm e} = 0.05$, $\epsilon_{\rm e} = 0.01$, and $\epsilon_B = 0.001$.

3 RESULTS

3.1 Light curves and spectra

We consider bursts with outburst energy of $\mathcal{E}_k = 10^{42} - 10^{47}$ erg and assume that the outflows are largely isotropic. For observed GRBs that presumably originate from MGFs, such as GRB 200415A, according to the summary of Burns et al. (2021), the range of their isotropic energy is from a few 10^{44} to 10^{46} erg. Considering the relationship between kinetic energy and isotropic energy, the energy interval we choose is reasonable. The quasi-isotropic assumption is also reasonable for MGFs although the isotropic-equivalent energy can be larger if beamed. In the following sections, we present our results based on numerical calculations with $s = 2.2$ and $\Gamma_0 = 2$.

Bhardwaj et al. (2021) reported a repeating FRB 20200120E and they suggested that M 81, which is a spiral galaxy at 3.63 ± 0.34 Mpc, is the most likely host of FRB 20200120E. We then consider there is a burst that occurred at $d_{\rm L} = 4$ Mpc which is similar to the luminosity distance of galaxy M 81.

3.1.1 Thin shell

In Fig. 4, we show the light curves of the observed flux at 1 and 100 GHz, respectively. The kinetic energy of the burst is assumed to be $\mathcal{E}_k = 10^{44}$ erg. For comparison, we also consider the case with $\mathcal{E}_k = 10^{47}$ erg even though it is rare for bursts related to MGFs and/or FRBs. As shown in the previous section, the external baryonic ejecta density has a significant effect on the observed flux due to the SSA and FF effect, and it is determined by the mass of the SN ejecta $M_{\rm ext}$ and the age of the magnetar $T_{\rm age}$ as shown in equation (3). In this work, we fix $M_{\rm ext} = 10\,{\rm M}_\odot$, which is reasonable for SN ejecta. Considering the uncertainty of the onset time of the MGFs and/or FRBs since SN explosion, we consider $T_{\rm age} = 10,\ 30,\ 100$, and 300 yr, respectively. Note that the shock will turn into the radiative phase when $t = t_{\rm cool}$ (e.g. Blondin et al. 1998), where $t_{\rm cool} \simeq 0.69 k T_{\rm sh}/(n_{\rm ext}\Lambda_{\rm cool})$ is the cooling time, $\Lambda_{\rm cool} \sim 10^{-16}$ erg cm^3 s^{-1} $T_{\rm sh}^{-1}$ is the temperature-dependent volume cooling function, $T_{\rm sh} \simeq 1.9 \times 10^{10}$ K $\mathcal{E}_{k,47}^{2/5} n_{\rm ext,3}^{-2/5} t_6^{-6/5}$ is the temperature of the shock-heated gas for an adiabatic shock. Noting that the shock crossing time is comparable to the dynamical time $t_{\rm dyn} \approx r_{\rm s}/v_{\rm s}$, the transition time from the adiabatic phase to the radiative

Downloaded from https://academic.oup.com/mnras/article/524/4/6004/7224608 by guest on 09 August 2023

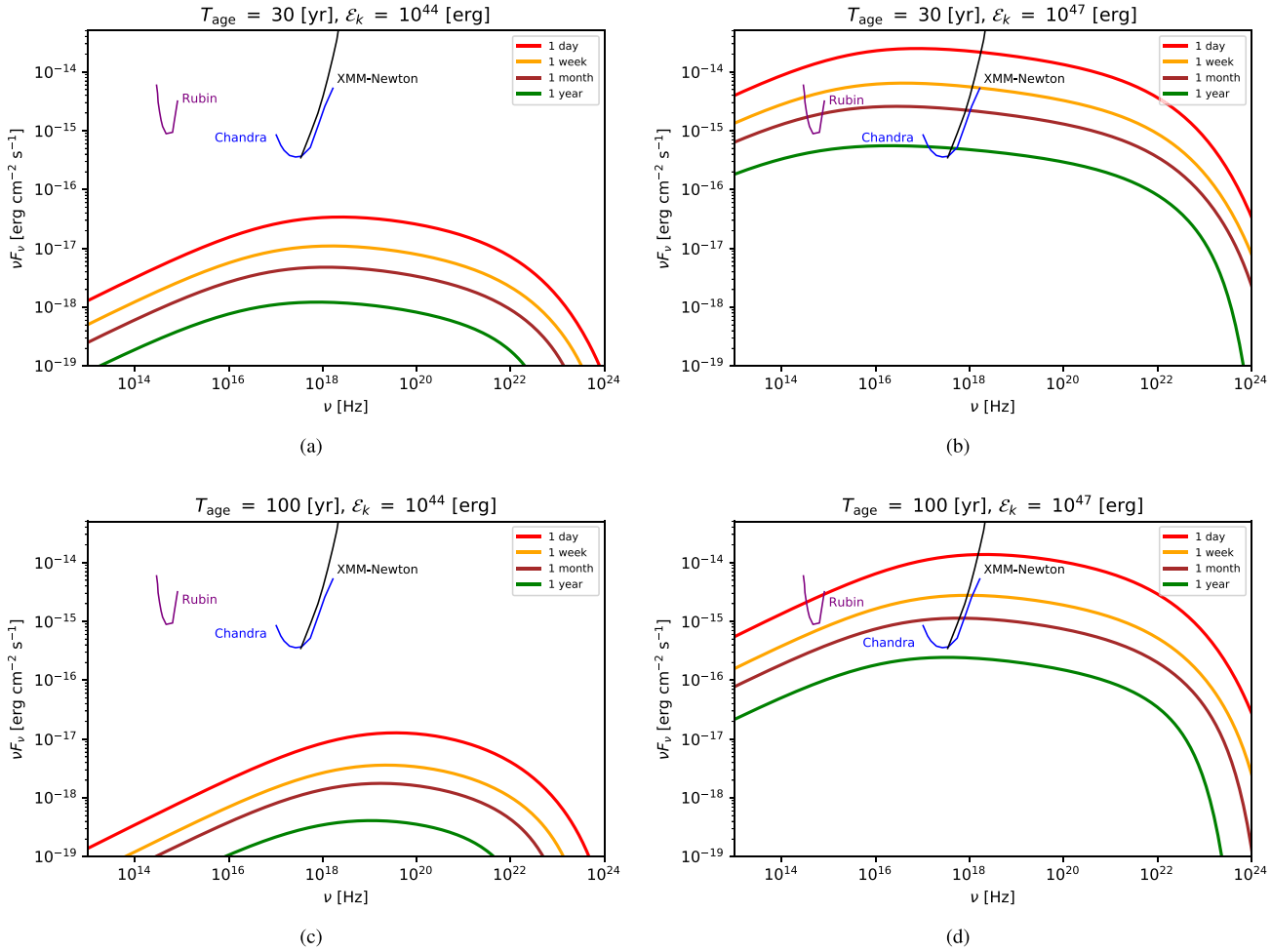

Figure 5. Energy spectra of the afterglow emission predicted in the burst-in-bubble model for $\mathcal{E}_k = 10^{44}$ erg (left-hand panel) and 10^{47} erg (right-hand panel), respectively. The sensitivity curves of *Chandra* (blue line) and *XMM–Newton* (black line) are calculated with an exposure time of 10^5 s (Lucchetta et al. 2022). The purple lines show the r-band sensitivity of the Vera C. Rubin Observatory with a point source exposure time of 30 s in the 3 d revisit time (Yuan et al. 2021). In the upper panels and lower panels, we set T_{age} to be 30 and 100 yr, respectively. The corresponding physical parameters are $\Gamma_0 = 2$, $d_L = 4$ Mpc, $s = 2.2$, $f_e = 0.05$, $\epsilon_e = 0.01$, and $\epsilon_B = 0.001$.

phase is $t_{tr} \simeq 59$ yr $\mathcal{E}_{k,47}^{4/17} n_{ext,3}^{-9/17}$. For $T_{age} = 10$–100 yr, the radiative transition time is $\sim$ 1–10 yr. Therefore, we just show the light curves at $t \leq 10$ yr.

The sensitivity of current and next-generation radio telescopes are considered.[2] For VLA and ALMA, the root-mean-square (RMS) sensitivities could be obtained using the calculators[3] with exposure time $t_{exp} = 10^4$ s. For SKA and ngVLA, we found the RMS sensitivities with $t_{exp} = 3600$ s from their official websites, and the corresponding RMS with $t_{exp} = 10^4$ s could be derived using the relation RMS $\propto t_{exp}^{-1/2}$. The 3σ upper limits $S = 3$ RMS are indicated as black lines in Fig. 4, which are 16.0 μJy (for VLA at 1 GHz), 3.6 μJy (for SKA at 1 GHz), 19.7 μJy (for ALMA at 100 GHz), and 0.72 μJy (for ngVLA at 100 GHz), respectively.

In Figs 4(a) and (c), we show the light curve with $\mathcal{E}_k = 10^{44}$ erg. We can see that the afterglow emission with $T_{age} = 10$ and 30 yr at $\nu = 1$ GHz is almost reduced to zero since the FF absorption is strong when T_{age} becomes smaller. Due to the smaller value of the burst kinetic energy, the detection is still difficult even with larger T_{age} where the FF absorption could be neglected. However, the detection of the afterglow emission for ngVLA at $\nu = 100$ GHz is possible at earlier time $t \lesssim 1.0 \times 10^4$ s if $T_{age} = 30$ yr where the effect of FF absorption is not important at higher frequency band. In Figs 4(b) and (d), we show the light curve with $\mathcal{E}_k = 10^{47}$ erg. Different from the previous case, both VLA and SKA could detect the afterglow emission with $T_{age} = 100$ and 300 yr for $\nu = 1$ GHz. For $\nu = 100$ GHz, the afterglow with $T_{age} = 10$–300 yr could be detected by ngVLA, but for ALMA detecting the afterglow with $T_{age} = 300$ yr is difficult. Note that the increase of the light curve in Fig. 4(d) with $T_{age} = 10$ yr (red solid line) in late time is due to the gradual weakening of FF absorption when the forward shock propagates near the edge of the external baryonic ejecta (that is $r_s/R_{ext} \sim 30$ per cent).

In Fig. 5, we show the energy spectra of the afterglow emission for $\mathcal{E}_k = 10^{44}$ erg (left-hand panel) and $\mathcal{E}_k = 10^{47}$ erg (right-hand panel) at different observation times from one day to one year. In the upper panels and lower panels, we show the spectra with $T_{age} = 30$ and 100 yr, respectively. At the X-ray band, we added the sensitivity

[2]The official website of these radio telescopes: VLA (http://www.vla.nrao.edu), SKA (https://www.skatelescope.org), ALMA (https://public.nrao.edu/telescopes/alma/), and ngVLA (https://ngvla.nrao.edu/).

[3]The calculator website of VLA: https://obs.vla.nrao.edu/ect, and that of ALMA: https://almascience.nrao.edu/proposing/sensitivity-calculator.

Downloaded from https://academic.oup.com/mnras/article/524/4/6004/7224608 by guest on 09 August 2023

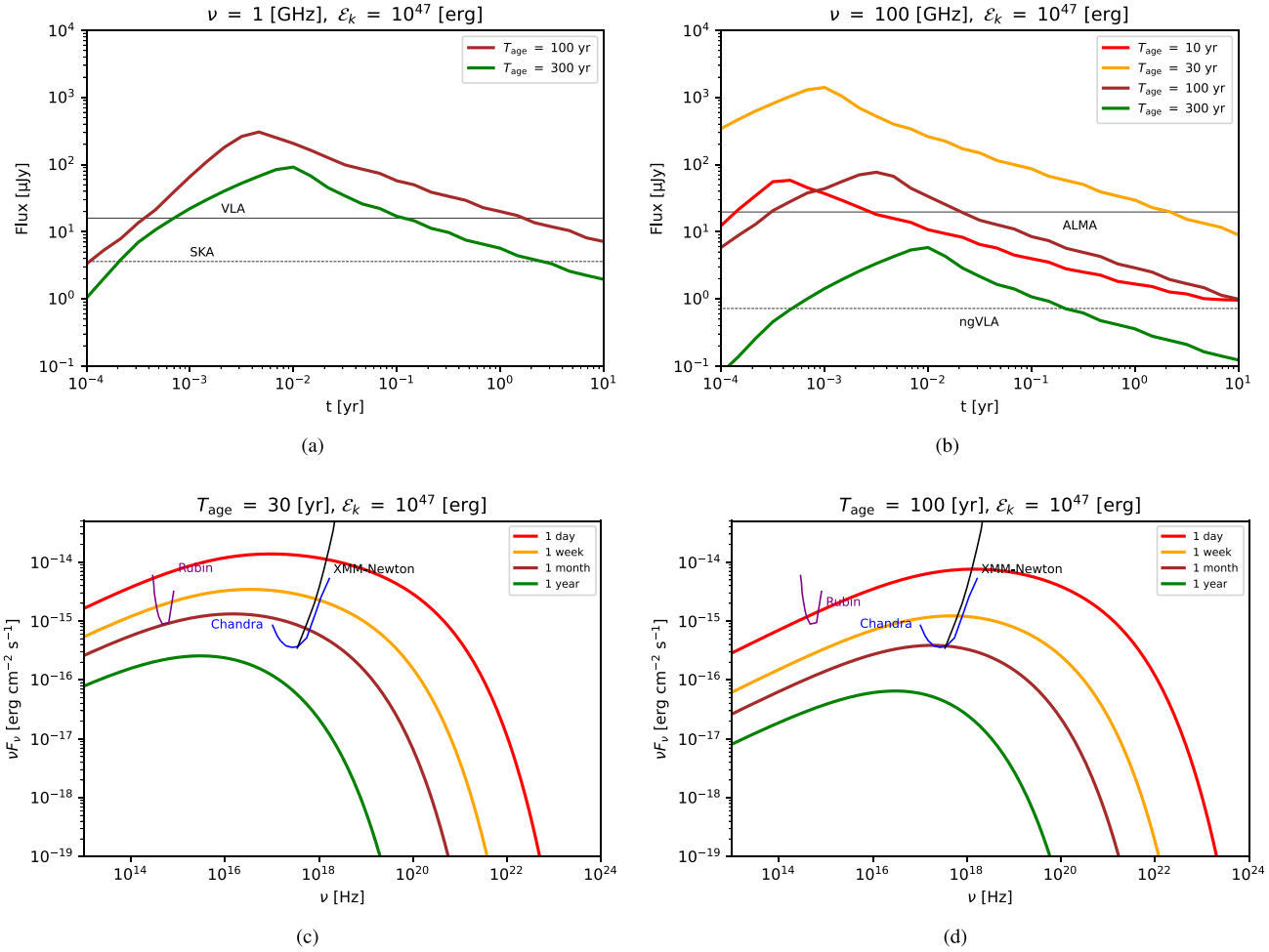

Figure 6. Light curves (upper panels) and energy spectra (lower panels) of FRB afterglow emission with $\mathcal{E}_k = 10^{47}$ erg, respectively. The corresponding physical parameters are $\Gamma_0 = 2$, $d_L = 4$ Mpc, $s = 2.2$, $f_e = 0.05$, $\epsilon_e = 0.01$, and $\epsilon_B = 0.001$.

curves of *Chandra* (blue curve) and *XMM–Newton* (black curve) which are calculated with an exposure time of 10^5 s. We can see that the detection of the afterglow emission with $T_{age} = 30$ yr (100 yr) at the X-ray band is promising for $\mathcal{E}_k = 10^{47}$ erg when the observation time ranges from 1 d to 1 yr (1 month), but the X-ray flux is too low to be detected for $\mathcal{E}_k = 10^{44}$ erg. However, the X-ray emission may not be detected since the neutral SN ejecta could absorb the X-ray emission even for $\mathcal{E}_k = 10^{47}$ erg. In order to judge the significance of the X-ray absorption, we calculate the column density $N_{ext} \approx (R_{ext} - r_s)n_{ext}$ assuming the SN ejecta are uniformly distributed. For $T_{age} = 30$ yr, we can get $N_{ext} \simeq 3.2 \times 10^{22}$ cm^{-2} (3.0×10^{22} cm^{-2}) for $t = 1$ d (1 yr) where the corresponding external baryonic number density is $n_{ext} \simeq 1.1 \times 10^5$ cm^{-3}. For hydrogen gas, the effect of X-ray absorption can be neglected if the column density is smaller than $K_X/m_H \sim 6.7 \times 10^{21}$ cm^{-2} $(h\nu/10\,\mathrm{keV})^{-3}$ (e.g. Murase et al. 2015). Our results indicate that it is possible for *XMM–Newton* and *Chandra* to detect the afterglow emission in the hard X-ray band.

We also show the sensitivity curve of the Vera C. Rubin Observatory in Fig. 5. The detection with the Vera C. Rubin Observatory at the optical band is promising for $\mathcal{E}_k = 10^{47}$ erg at $t \lesssim 1$ month (1 d) for $T_{age} = 30$ yr (100 yr). For the fluxes with $\mathcal{E}_k = 10^{44}$ erg, they would be too faint to be detected with the Vera C. Rubin Observatory.

3.1.2 *Thick shell*

The typical value of the nebula width ΔR_{ej} could be estimated as

$$\Delta R_{ej} = \frac{R_{nb}}{12\Gamma_0^2} \simeq 2.1 \times 10^{14}\ \mathrm{cm}\ R_{nb,16}, \tag{18}$$

where $R_{nb} \simeq 1.6 \times 10^{16}$ cm $P_{i,0}^{-2/5} M_{ext,1M_\odot}^{-1/5} V_{ext,8.5}^{3/5} T_{age,10yr}$ is the radius of nebula (e.g. Murase et al. 2016), and P_i is the initial rotation period of magnetar. When the inner ejecta propagates into the SN baryonic ejecta and spreading is negligible, the reverse shock finishes crossing the inner ejecta at the shock crossing time

$$t_{cross} = \frac{\Delta R_{ej}}{v_0} \simeq 1.3 \times 10^4\ \mathrm{s}\ R_{nb,16}. \tag{19}$$

If $t_{cross} > t_{dec}$, the thin-shell approximation is not valid, where the observed flux peaks at $t_\times \approx t_{cross}$. Here, we consider the thick-shell approximation.

In the upper panels of Fig. 6, we show the light curves with $\mathcal{E}_k = 10^{47}$ erg at 1 GHz (left-hand panel) and 100 GHz (right-hand panel) for the thick-shell approximation. Compared with Figs 4(b) and 4(d), we see that the late-time fluxes are similar. However, the fluxes peak at later times around t_{cross}, and the relative fluxes around the peak are lower than those in the thin-shell approximation by a factor of ∼1–5. For 1 GHz, VLA and SKA

Downloaded from https://academic.oup.com/mnras/article/524/4/6004/7224608 by guest on 09 August 2023

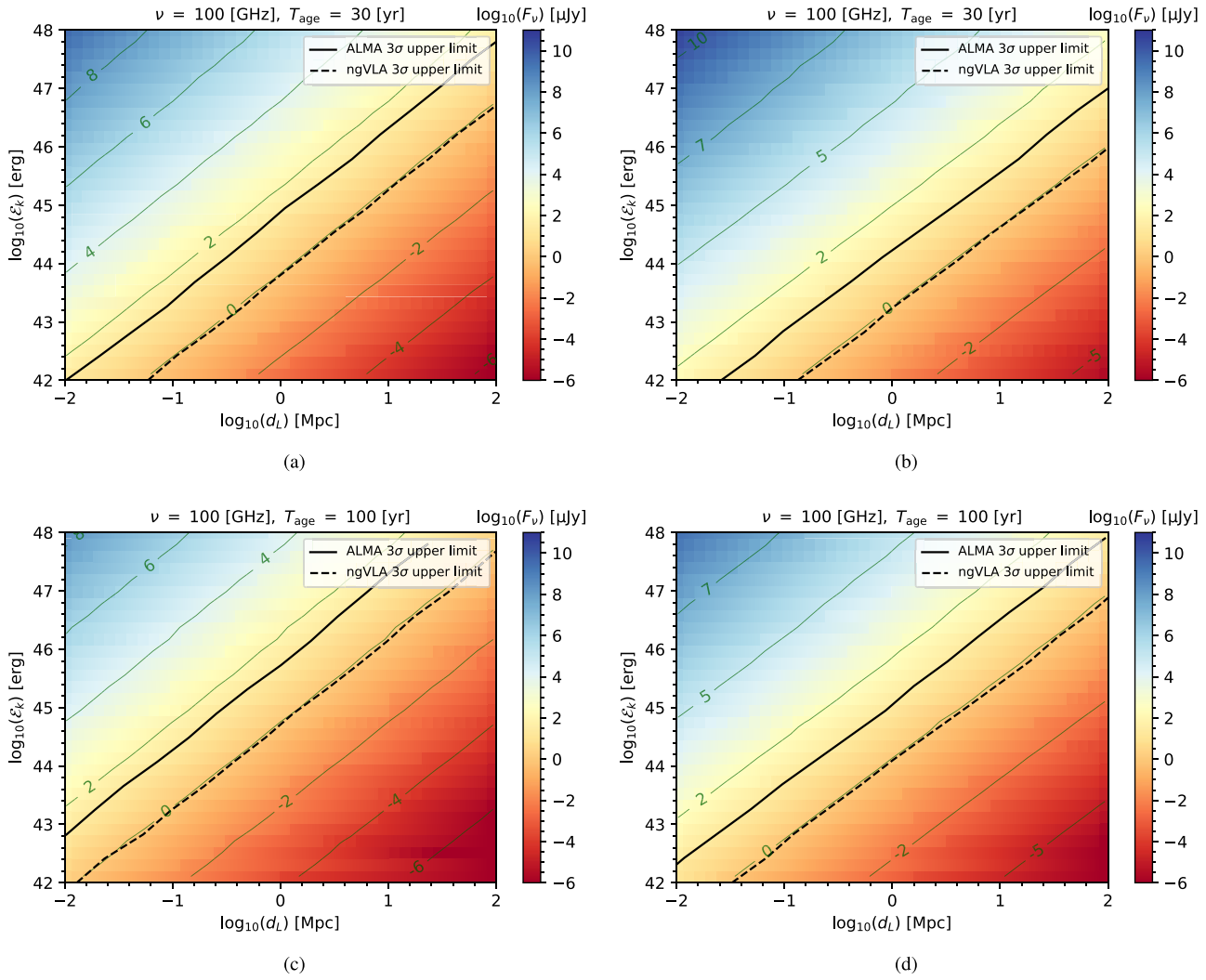

Figure 7. Parameter space in the $d_L - \mathcal{E}_k$ plane with the colour indicating the observed flux at 100 GHz with $s = 2.2$. The corresponding microphysical parameters are $f_e = 0.05, \epsilon_e = 0.01$, and $\epsilon_B = 0.001$ (left-hand panels), and $f_e = 0.1, \epsilon_e = 0.1$, and $\epsilon_B = 0.1$ (right-hand panels). The kinetic energy has range $\mathcal{E}_k = 10^{42}$–10^{48} erg, while the distance ranging from $d_L = 10^{-2}$–10^2 Mpc. In each plot, the green lines are the contour lines in which we write the corresponding value of flux, and the solid and dashed black lines mean the sensitivity of the radio telescopes. In the upper panels and lower panels, we set T_{age} to be 30 and 100 yr, respectively.

can detect the afterglow with $T_{age} = 100$–300 yr. For 100 GHz, ALMA (ngVLA) can detect the afterglow with $T_{age} = 10$–100 yr ($T_{age} = 10$–300 yr).

In the lower panels of Fig. 6, we show the spectra with $\mathcal{E}_k = 10^{47}$ erg for $T_{age} = 30$ (left-hand panel) and $T_{age} = 100$ yr (right-hand panel). At the X-ray band, *XMM–Newton* and *Chandra* may detect afterglow emission with $t \lesssim 1$ month for $T_{age} = 30$ and 100 yr. At the optical band, it is possible for the Vera C. Rubin Observatory to detect afterglow with $t \lesssim 1$ month ($t \lesssim 1$ d) for $T_{age} = 30$ yr ($T_{age} = 100$ yr).

3.2 Detection horizon for radio afterglows

In the following sections, we adopt the thick-shell approximation to perform the calculations.

The detectability of afterglow emission is affected by $\mathcal{E}_k$. For a given burst kinetic energy, the detection horizon $d_{L,\rm lim}$ considering the sensitivity curves of radio telescopes is given by

$$d_{L,\rm lim} = \left(\frac{\nu L_\nu(t_{\rm peak})}{4\pi F_{\rm lim}}\right)^{1/2}, \tag{20}$$

where $\nu L_\nu(t_{\rm peak})$ is the observed luminosity at $t = t_{\rm peak}$, $t_{\rm peak}$ is the time when the luminosity reaches maximum value during the time interval from $10^{-3.5}$ to 10^2 yr, and $F_{\rm lim}$ is the detector sensitivity at a given frequency. In Fig. 7, the detection horizon at 100 GHz for ALMA (solid curve) and ngVLA (dashed curve) are indicated as black curves in the $d_L - \mathcal{E}_k$ plane where the colour indicates the flux observed at $t_{\rm peak}$, respectively. The green contours are the corresponding values of the logarithm of the observed fluxes.

In the left-hand panels, we show the results for $f_e = 0.05$, $\epsilon_e = 0.01$, and $\epsilon_B = 0.001$, which can be regarded as the conservative case. We see that the corresponding detection horizon is more extensive for $T_{age} = 30$ than 100 yr for both ALMA and ngVLA. The detection horizon is larger for ngVLA compared to ALMA. For example, in

Downloaded from https://academic.oup.com/mnras/article/524/4/6004/7224608 by guest on 09 August 2023

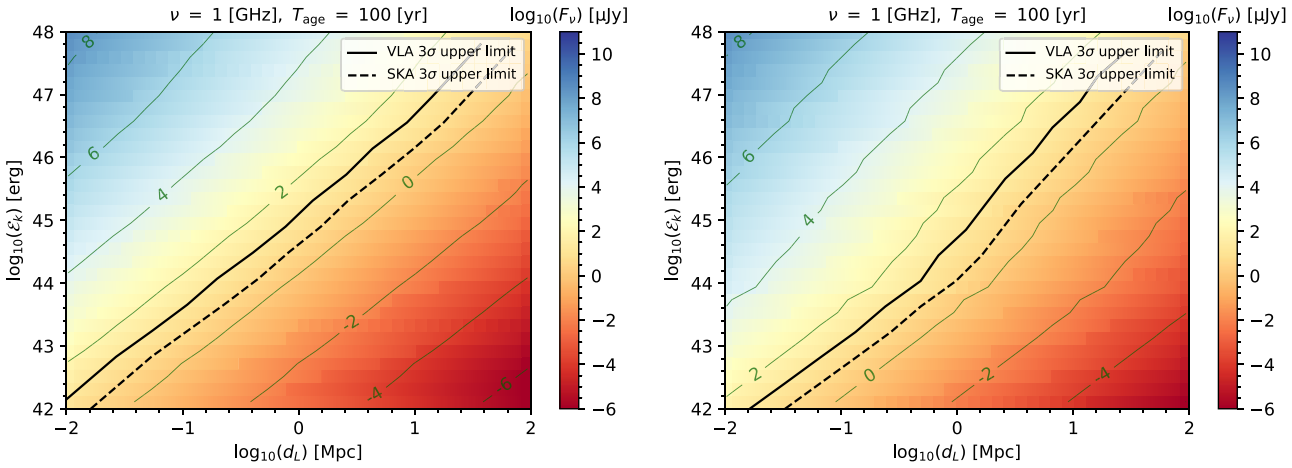

Figure 8. Similar to Fig. 7, the colour indicates the observed flux at 1 GHz with $s = 2.2$. The corresponding microphysical parameters are $f_e = 0.05, \epsilon_e = 0.01$, and $\epsilon_B = 0.001$ (left-hand panel), and $f_e = 0.1, \epsilon_e = 0.1$, and $\epsilon_B = 0.1$ (right-hand panel).

Fig. 7(a), the values of $d_{L,lim}$ for $T_{age} = 30$ yr are 0.01 Mpc (0.06 Mpc) for $\mathcal{E}_k = 10^{42}$ erg, 1.2 Mpc (6.7 Mpc) for $\mathcal{E}_k = 10^{45}$ erg and 59 Mpc (310 Mpc) for $\mathcal{E}_k = 10^{47.5}$ erg for ALMA (ngVLA), respectively.

In the right-hand panels, we show the results for $f_e = 0.1$, $\epsilon_e = 0.1$, and $\epsilon_B = 0.1$, in which the detection horizon becomes larger. For example, in Fig. 7(b), the values of $d_{L,lim}$ for $T_{age} = 30$ yr are 0.026 Mpc (0.13 Mpc) for $\mathcal{E}_k = 10^{42}$ erg, 3.8 Mpc (20 Mpc) for $\mathcal{E}_k = 10^{45}$ erg and 190 Mpc (980 Mpc) for $\mathcal{E}_k = 10^{47.5}$ erg for ALMA (ngVLA), respectively.

In Fig. 8, we show similar plots for $\nu = 1$ GHz. Because the observed flux at 1 GHz is more strongly affected by the effect of FF absorption than that at 100 GHz for $T_{age} = 30$ yr, we only show the results for $T_{age} = 100$ yr. The detection horizons at the 1 GHz band for VLA (solid curve) and SKA (dashed curve) are indicated as black curves in the d_L–$\mathcal{E}_k$ plane. Contrary to the 100 GHz band, the detection horizon at the 1 GHz band is comparable for bursts with a kinetic energy of $\mathcal{E}_k \gtrsim 10^{45}$ erg for both parameter sets of the microphysical parameters.

3.3 Expected numbers of afterglows detected with current and next-generation radio telescopes

The total number of detectable events, N_{burst}, could be obtained from the following equation

$$N_{burst} = \Delta T \int_{\mathcal{E}_{k,min}}^{\mathcal{E}_{k,max}} d\mathcal{E}_k \int_0^{d_{L,lim}(\mathcal{E}_k)} dd_L 4\pi d_L^2 \frac{dR_{burst}}{d\mathcal{E}_k}, \quad (21)$$

where ΔT is the observation time of the telescope, $\mathcal{E}_{k,min}$ is the minimum kinetic energy, $\mathcal{E}_{k,max}$ is the maximum kinetic energy, $d_{L,lim}(\mathcal{E}_k)$ is the detection horizon for a given $\mathcal{E}_k$ and $dR_{burst}/d\mathcal{E}_k$ is the differential event rate of the bursts.

3.3.1 MGF scenario

In this section, we consider bursts driven by MGFs. According to Burns et al. (2021), the best-fitting volumetric rate of MGFs is $R_{MGF} \approx 3.8 \times 10^5\,\mathrm{Gpc^{-3}\,yr^{-1}}$ assuming the energy distribution of MGFs follows a power-law distribution with spectral index $\alpha \approx 1.7$. The lowest considered value of the isotropic-equivalent energy of the MGFs is $\mathcal{E}_{iso,min} = 3.7 \times 10^{44}$ erg and the maximum isotropic-equivalent energy could be as high as $\mathcal{E}_{iso,max} = 5.75 \times 10^{47}$ erg (Burns et al. 2021). Here, we assume $\mathcal{E}_k \approx \mathcal{E}_{iso}$. This is conservative in the sense that the radiative efficiency is less than unity, e.g. $\mathcal{E}_k \sim 5\mathcal{E}_{iso}$ for GRBs (e.g. Kumar & Zhang 2014). For a given age T_{age}, the burst rate density $dR_{burst}/d\mathcal{E}_k$ can be estimated as

$$\frac{dR_{burst}|_{T_{age}}}{d\mathcal{E}_k} = f_{age} R_{MGF} \frac{(1-\alpha)\mathcal{E}_k^{-\alpha}}{\mathcal{E}_{iso,max}^{1-\alpha} - \mathcal{E}_{iso,min}^{1-\alpha}}, \quad (22)$$

where $f_{age} = T_{age}/T_{life}$ represents the fraction of magnetars with T_{age} and $T_{life} \sim 10^4$ yr is the typical life time of magnetars (e.g. Kaspi & Beloborodov 2017). We assume that the value of f_{age} is 0.01 for $T_{age} = 100$ yr while it is 0.003 for $T_{age} = 30$ yr.

Table 1. Expectation numbers of detectable afterglow events. The observational time window of radio telescopes is assumed to be $\Delta T = 10$ yr. In the upper and lower parts, we assume $f_e = 0.05$, $\epsilon_e = 0.01$, and $\epsilon_B = 0.001$, and $f_e = 0.1$, $\epsilon_e = 0.1$, and $\epsilon_B = 0.1$, respectively.

ν \ T_{age}		30 yr	100 yr
1 GHz	VLA	0	0.020
	SKA	0	0.17
100 GHz	ALMA	0.054	0.0021
	ngVLA	7.6	0.35
ν \ T_{age}		30 yr	100 yr
1 GHz	VLA	0	0.013
	SKA	0	0.13
100 GHz	ALMA	2.0	0.086
	ngVLA	270	12

In Table 1, we show the total number of detected events using equation (21) and (22) with $\Delta T = 10$ yr. We can see that the expected detection number is more prominent at the 100 GHz band by ALMA and ngVLA. In particular, ngVLA could detect $N_{burst} \sim 7.6$ for $T_{age} = 30$ yr and $N_{burst} \sim 0.35$ for $T_{age} = 100$ yr in the conservative case, while the corresponding number is ~35 times larger for $f_e = 0.1, \epsilon_e = 0.1$, and $\epsilon_B = 0.1$. The detection number with ALMA is expected to be $N_{burst} \sim 2$ for $f_e = 0.1, \epsilon_e = 0.1$, and $\epsilon_B = 0.1$ with $T_{age} = 30$ yr. At the 1 GHz band, the expected detection number is less than unity for both VLA and SKA with $\Delta T = 10$ yr. The results are consistent with

Downloaded from https://academic.oup.com/mnras/article/524/4/6004/7224608 by guest on 09 August 2023

Table 2. Similar to Table 1, but the difference is that here we assume that the observation is conducted 1 d after the burst.

ν \ T_{age}		30 yr	100 yr
1 GHz	VLA	0	0.020
	SKA	0	0.17
100 GHz	ALMA	0.0085	0.0021
	ngVLA	1.4	0.35

ν \ T_{age}		30 yr	100 yr
1 GHz	VLA	0	0.013
	SKA	0	0.13
100 GHz	ALMA	0.21	0.085
	ngVLA	36	12

the conclusions derived in the previous section where the detection at the 1 GHz band for smaller $T_{\rm age}$ is largely affected by the effect of FF absorption. Note the effect of FF absorption could be reduced considering the spatial distribution of the SN ejecta is asymmetric or clumpy, where a fraction of photons are expected to escape freely.

Because the observation time of radio telescopes cannot be easily adjusted to the peak time of afterglow emission, we calculate the total number of detected events assuming that the observation is conducted 1 d after the burst, for which the results are shown in Table 2. We find that the corresponding values of $N_{\rm burst}$ are decreased by a factor ∼1–10, but the expected detection number for ngVLA at the 100 GHz band could be $N_{\rm burst} \gtrsim 1$.

3.3.2 *FRB scenario*

In this section, we consider the scenario, in which bursts are associated with FRBs. The burst rate density $\mathrm{d}R_{\rm burst}/\mathrm{d}\mathcal{E}_k$ can be estimated as

$$\frac{\mathrm{d}R_{\rm burst}|_{T_{\rm age}}}{\mathrm{d}\mathcal{E}_k} = f_{\rm age} R_{\rm FRB} \frac{\mathcal{E}_k^{-\alpha}}{\mathcal{E}_{k,\rm cr}^{1-\alpha}}, \quad (23)$$

where $R_{\rm FRB} \approx 339\,{\rm Gpc^{-3}\,yr^{-1}}$ is the characteristic volumetric rate of FRBs at $\mathcal{E}_{k,\rm cr}$, where $\mathcal{E}_{k,\rm cr}$ is the critical kinetic energy and $\alpha \approx 1.79$ is the index (Luo et al. 2020). The critical energy can be estimated as $\mathcal{E}_{k,\rm cr} = (\delta t/\eta_{\rm FRB})L_{\rm cr} \sim 2.9 \times 10^{46}$ erg with $\delta t/\eta_{\rm FRB} = 100$ s, where δt is the duration of FRB, $\eta_{\rm FRB}$ is the radiative efficiency and $\log_{10}(L_{\rm cr}[\ {\rm erg\ s^{-1}}]) \simeq 44.46$ is the logarithmic of the critical luminosity of GRB (Luo et al. 2020). Here we use $\mathcal{E}_{k,\rm min} = 10^{42}$ and $10^{47.5}$ erg to calculate $N_{\rm burst}$.

The results are summarized in Tables 3–4. Compared to Tables 1–2, the total number of detectable afterglow events decreases by a factor of ∼50, which is consistent with the difference in the measured volumetric rate between MGFs and FRBs adopted in this work.

4 SUMMARY AND DISCUSSION

In this work, we performed detailed studies on the afterglow emission caused by bursts that may be related to MGFs or FRBs occurring in their wind nebulae and surrounding baryonic ejecta. Based on the bursts-in-bubble model, we used both analytical and numerical methods to calculate the dynamical evolution of the trans-relativistic shell formed when the nebula swept by the burst-driven outflow propagates within the dense baryonic ejecta, and the energy spectra and light curves of the afterglow emission from refreshed forward shock. We adopted the thick-shell approximation considering the merged shell has an initial width $\Delta R_{\rm ej}$ after compressed by the FRB and/or MGF bursts.

Table 3. Similar to Table 1, but the detection number $N_{\rm burst}$ is obtained by assuming that the burst is driven by an FRB with $\Delta T = 10$ yr.

ν \ T_{age}		30 yr	100 yr
1 GHz	VLA	0	4.8×10^{-4}
	SKA	0	0.0041
100 GHz	ALMA	0.0012	5.0×10^{-5}
	ngVLA	0.18	0.0081

ν \ T_{age}		30 yr	100 yr
1 GHz	VLA	0	3.2×10^{-4}
	SKA	0	0.0032
100 GHz	ALMA	0.046	0.0020
	ngVLA	6.3	0.28

Table 4. Similar to Table 3, but the difference is that here we assume that the observation is conducted 1 d after the burst.

ν \ T_{age}		30 yr	100 yr
1 GHz	VLA	0	4.8×10^{-4}
	SKA	0	0.0041
100 GHz	ALMA	2.0×10^{-4}	4.9×10^{-5}
	ngVLA	0.033	0.0080

ν \ T_{age}		30 yr	100 yr
1 GHz	VLA	0	3.2×10^{-4}
	SKA	0	0.0032
100 GHz	ALMA	0.0049	0.0020
	ngVLA	0.82	0.27

Motivated by the detection of FRB 20200120E, we calculated the light curves and spectra assuming there is a burst occurred at $d_{\rm L} = 4$ Mpc with different kinetic-energy $\mathcal{E}_k$ and age $T_{\rm age}$. The detection of the afterglow emission for energetic bursts with $\mathcal{E}_k = 10^{47}$ erg is promising, where the flux is above the detection threshold of current and next-generation radio telescopes for reasonable values of $T_{\rm age}$. Due to FF absorption, the detection of the afterglow emission with VLA and SKA at the 1 GHz band would be challenging when $T_{\rm age} \lesssim 30$ yr.

We also studied the detectability of afterglow with current X-ray telescopes, such as *Chandra* and *XMM–Newton*. Our results show that the X-ray telescopes have the ability to detect X-ray afterglow emission with $T_{\rm age} = 30$ and 100 yr at $t \lesssim 1$ month for $\mathcal{E}_k = 10^{47}$ erg. The detection of the afterglow with $T_{\rm age} = 30$ yr (100 yr) at the optical band with the Vera C. Rubin Observatory is also promising at $t \lesssim 1$ month (1 d) for $\mathcal{E}_k = 10^{47}$ erg. The joint observations at the multiwavelength bands, including radio, optical, and X-ray, will allow us to unveil the details of the bursts-in-bubble model.

We then studied the detection horizon and expected number of events with current and next-generation radio telescopes. We found the detection horizon $d_{\rm L,\ lim}$ could range from 0.010 (0.059) to 59 Mpc (310 Mpc) for bursts with kinetic energy from 10^{42} to $10^{47.5}$ erg for ALMA (ngVLA). The detection horizon could be larger for microphysical parameters $f_{\rm e} = 0.1$, $\epsilon_{\rm e} = 0.1$, and $\epsilon_B = 0.1$. The detection horizon at 1 GHz band with VLA and SKA is also

Downloaded from https://academic.oup.com/mnras/article/524/4/6004/7224608 by guest on 09 August 2023

promising for energetic bursts, except for the effect of FF absorption when $T_{\rm age} \lesssim 30$ yr.

We calculated the number of detectable afterglow events for current and next-generation radio telescopes, as shown in Section 3.3. If we assume that the burst rate follows MGFs, the expected numbers of burst afterglows for ALMA and ngVLA could be larger than unity with a few decades of operation. In the FRB scenario, the expected numbers would be less, but ngVLA has the possibility to detect the afterglow emission within a few ten years. However, radio telescopes such as ngVLA and ALMA cannot follow up on a burst immediately, so we also consider the observation is conducted 1 d after the burst, as shown in Table 2 and Table 4. We found the detection number becomes smaller than the ideal case, but still possible for ngVLA to detect the afterglow driven by MGFs and/or FRBs with suitable parameters within a few ten years. Our theoretical expectation regarding the number of afterglows detected with ALMA and VLA is consistent with the current observation that no similar signals are detected by these two radio telescopes. Note that our results on the expected numbers of afterglow depend on $T_{\rm age}$, and here we just show the results with $T_{\rm age} = 30$ and 100 yr. The values of $\mathcal{E}_{k,\rm min}$ and $\mathcal{E}_{k,\rm max}$ we adopted in this work for both MGFs and FRBs could affect the number of detected events, where future observations are needed to unveil the mysteries.

In this study, we focused on the forward shock component in afterglow emission. In addition, the reverse shock component could be significant in the thick-shell limit around $t_\times \approx t_{\rm cross}$, which could enhance the flux at the radio band. The afterglow emission may also be outshined by the quasi-steady nebular emission. According to Murase et al. (2016), if the nebula is powered by magnetar rotation, the observed energy flux of the nebular emission $\nu F_\nu^{\rm nb}$ depends on the spin-down power of the magnetar $L_{\rm sd} \simeq 2.4 \times 10^{39} B_{*,15}^2 P_{-0.5}^{-4}$ erg s^{-1}, where B_* is the magnetic field of magnetar, $P = P_i(1 + T_{\rm age}/T_{\rm sd})^{1/2}$ is the rotation period of magnetar, P_i is the initial rotation period and $T_{\rm sd} \simeq 2.5$ yr $B_{*,15}^{-2} P_{i,-0.5}^2$ is the spin-down time. We found with $P_i = 1$–10 s, the nebular emission can be lower than afterglow fluxes for energetic bursts with $\mathcal{E}_k \gtrsim 10^{44} - 10^{45}$ erg given that $f_{\rm e} = 0.1$, $\epsilon_{\rm e} = 0.1$, and $\epsilon_B = 0.1$. The nebular emission is model dependent, and the number of detectable afterglow events would be dominated by sufficiently energetic bursts, in which the nebular component is subdominant.

ACKNOWLEDGEMENTS

We acknowledge the anonymous referee for valuable comments. The work was partly supported by the NSF grant nos. AST-1908689, AST-2108466 and AST-2108467, and KAKENHI No. 20H01901 and No. 20H05852 (KM).

DATA AVAILABILITY

The data developed for the calculation in this work is available upon request.

REFERENCES

Acciari V. A., et al., 2018, MNRAS, 481, 2479
Asano K., Murase K., Toma K., 2020, ApJ, 905, 105
Bhardwaj M. et al., 2021, ApJ, 910, L18
Blondin J. M., Wright E. B., Borkowski K. J., Reynolds S. P., 1998, ApJ, 500, 342
Bochenek C. D., Ravi V., Belov K. V., Hallinan G., Kocz J., Kulkarni S. R., McKenna D. L., 2020, Nature, 587, 59
Burns E. et al., 2021, ApJ, 907, L28
CHIME/FRB Collaboration, 2020, Nature, 587, 54
DeLaunay J. J. et al., 2016, ApJ, 832, L1
Dermer C. D., Menon G., 2009, High Energy Radiation from Black Holes: Gamma Rays, Cosmic Rays, and Neutrinos. Princeton Univ. Press, Princeton, NJ
Frederiks D. D., Golenetskii S. V., Palshin V. D., Aptekar R. L., Ilyinskii V. N., Oleinik F. P., Mazets E. P., Cline T. L., 2007, Astron. Lett., 33, 1
Gaensler B. M., Slane P. O., 2006, ARA&A, 44, 17
Granot J. et al., 2006, ApJ, 638, 391
Huang Y. F., Cheng K. S., 2003, MNRAS, 341, 263
Hurley K. et al., 1999, Nature, 397, 41
Kaspi V. M., Beloborodov A. M., 2017, ARA&A, 55, 261
Kumar P., Zhang B., 2014, Phys. Rept., 561, 1
Lang K. R., 1999, Astrophysical formulae. Springer, Berlin
Li L., Li Q.-C., Zhong S.-Q., Xia J., Xie L., Wang F.-Y., Dai Z.-G., 2022, ApJ, 929, 139
Lin H., Totani T., 2020, MNRAS, 498, 2384
Lucchetta G., Ackermann M., Berge D., Bühler R., 2022, J. Cosmol. Astropart. Phys., 2022, 013
Luo R., Men Y., Lee K., Wang W., Lorimer D. R., Zhang B., 2020, MNRAS, 494, 665
Lyubarsky Y., 2014, MNRAS, 442, L9
Martone R. et al., 2019, A&A, 631, A62
Matsumoto T., Piran T., 2021, MNRAS, 507, 4196
Mazets E. P., Golentskii S. V., Ilinskii V. N., Aptekar R. L., Guryan I. A., 1979, Nature, 282, 587
Mazets E. P., Cline T. L., Aptekar' R. L., Butterworth P. S., Frederiks D. D., Golenetskii S. V., Il'Inskii V. N., Pal'Shin V. D., 1999, Astron. Lett., 25, 635
Minaev P. Y., Pozanenko A. S., 2020, Astron. Lett., 46, 573
Mizuno Y., Pohl M., Niemiec J., Zhang B., Nishikawa K.-I., Hardee P. E., 2014, MNRAS, 439, 3490
Murase K., Toma K., Yamazaki R., Mészáros P., 2011, ApJ, 732, 77
Murase K., Kashiyama K., Kiuchi K., Bartos I., 2015, ApJ, 805, 82
Murase K., Kashiyama K., Mészáros P., 2016, MNRAS, 461, 1498
Murase K., Mészáros P., Fox D. B., 2017, ApJ, 836, L6
Nakar E., Piran T., 2011, Nature, 478, 82
Nava L., Sironi L., Ghisellini G., Celotti A., Ghirlanda G., 2013, MNRAS, 433, 2107
Nicastro L., Guidorzi C., Palazzi E., Zampieri L., Turatto M., Gardini A., 2021, Universe, 7, 76
Palmer D. M. et al., 2005, Nature, 434, 1107
Petroff E., Hessels J. W. T., Lorimer D. R., 2019, A&AR., 27, 4
Popov S. B., Postnov K. A., 2010, in Harutyunian H. A., Mickaelian A. M., Terzian Y., eds, Evolution of Cosmic Objects through their Physical Activity. Gitutyun Publishing House, NAS Republic of Armenia, p. 129
Roberts O. J. et al., 2021, Nature, 589, 207
Santana R., Barniol Duran R., Kumar P., 2014, ApJ, 785, 29
Sironi L., Giannios D., 2013, ApJ, 778, 107
Svinkin D. et al., 2021, Nature, 589, 211
Venere L. D., Principe G., Lalla N. D., Omodei N., Longo F., 2021, Proc. Sci., Gamma-ray emission from FRBs with Fermi-LAT , SISSA, Trieste, PoS#624
Yang J. et al., 2020, ApJ, 899, 106
Yi S.-X., Gao H., Zhang B., 2014, ApJ, 792, L21
Yuan C., Murase K., Zhang B. T., Kimura S. S., Mészáros P., 2021, ApJ, 911, L15
Zhang B., 2016, ApJ, 822, L14
Zhang B., 2022, preprint (arXiv:2212.03972)
Zhang B. T., Murase K., Veres P., Mészáros P., 2021, ApJ, 920, 55
Zhang B. B. et al., 2022, preprint (arXiv:2205.07670)

This paper has been typeset from a TEX/LATEX file prepared by the author.

© 2023 The Author(s)
Published by Oxford University Press on behalf of Royal Astronomical Society

Downloaded from https://academic.oup.com/mnras/article/524/4/6004/7224608 by guest on 09 August 2023